PCCP

PAPER

View Article Online
View Journal | View Issue

Published on 06 September 2017. Downloaded by Indiana University Libraries on 7/27/2018 11:48:17 AM.

Check for updates

Cite this: *Phys. Chem. Chem. Phys.*, 2017, **19**, 27801

Proton relays in anomalous carbocations dictate spectroscopy, stability, and mechanisms: case studies on $C_2H_5^+$ and $C_3H_3^+$†

LeeAnn M. Sager and Srinivasan S. Iyengar *

We present a detailed analysis of the anomalous carbocations: $C_2H_5^+$ and $C_3H_3^+$. This work involves (a) probing electronic structural properties, (b) *ab initio* dynamics simulations over a range of internal energies, (c) analysis of reduced dimensional potential surfaces directed along selected conformational transition pathways, (d) dynamically averaged vibrational spectra computed from *ab initio* dynamics trajectories, and (e) two-dimensional time–frequency analysis to probe conformational dynamics. Key findings are as follows: (i) as noted in our previous study on $C_2H_3^+$, it appears that these non-classical carbocations are stabilized by delocalized nuclear frameworks and "proton shuttles". We analyze this nuclear delocalization and find critical parallels between conformational changes in $C_2H_3^+$, $C_2H_5^+$, and $C_3H_3^+$. (ii) The vibrational signatures of $C_2H_5^+$ are dominated by the "bridge-proton" conformation, but also show critical contributions from the "classical" configuration, which is a transition state at almost all levels of theory. This result is further substantiated through two-dimensional time–frequency analysis and is at odds with earlier explanations of the experimental spectra, where frequencies close to the classical region were thought to arise from an impurity. While this is still possible, our results here indicate an additional (perhaps more likely) explanation that involves the "classical" isomer. (iii) Finally, in the case of $C_3H_3^+$ our explanation of the experimental result includes the presence of multiple, namely, "cyclic", "straight", and propargyl, configurations. Proton shuttles and nuclear delocalization, reminiscent of those seen in the case of $C_2H_3^+$, were seen all through and have a critical role in all our observations.

Received 15th August 2017,
Accepted 6th September 2017

DOI: 10.1039/c7cp05577c

rsc.li/pccp

I. Introduction

Anomalous carbocations have generated fundamental intrigue in physical organic chemistry for several decades.[1,2] These non-classical species are commonly seen in mass spectrometry experiments,[3] have a large presence in extra-terrestrial gas clouds,[4–6] and are proposed intermediates in several bio-synthetic pathways.[7–10] Anomalous carbocations defy the classical definition of chemical bonding and allow protons to remain delocalized between multiple carbon atoms, thus allowing multi-centered two-electron "bonds". There are several discussions in the literature[9–32] that emphasize the challenges these atypical bonding moieties present to electronic structure theory through the apparent, sometimes qualitative, disagreement between multiple levels of theory in predicting isomer stabilization energies. There are far fewer studies that take into account the dynamical nature of the nuclear framework[27,28,32] and still fewer that accurately account for nuclear quantization[29,31–33] due to the steep computational cost associated with these calculations.

In ref. 32, through the use of *ab initio* molecular dynamics (AIMD) and by inspecting critical quantum nuclear effects, it has been shown that the seemingly simple $C_2H_3^+$ carbocation is marked by delocalization and permutation of the three protons. This leads to a representation of the molecular structure where the three protons orbit the carbon skeleton in a fashion that is reminiscent of the "Grotthuss proton shuttle mechanism"[34] widely invoked for the study of proton transfer in water and in biological ion channels. This aspect was probed in ref. 32 using a combination of electronic structure calculations at multiple levels of theory, *ab initio* molecular dynamics simulations, and by exploring the effect of nuclear quantization through analysis of reduced-dimensional potential energy surfaces and by establishing the effect of H/D-isotope substitution. Vibrational properties were computed and the dynamical nature of the proton shuttle process was further probed by exploring two-dimensional (time–frequency) spectral signals. Nuclear quantum effects arising from the subsystem of protons were considered from the reduced dimensional potential surfaces mentioned above.

Department of Chemistry and Department of Physics, Indiana University, 800 E. Kirkwood Ave, Bloomington, IN-47405, USA. E-mail: iyengar@indiana.edu

† Electronic supplementary information (ESI) available. See DOI: 10.1039/c7cp05577c

Published on 06 September 2017. Downloaded by Indiana University Libraries on 7/27/2018 11:48:17 AM.

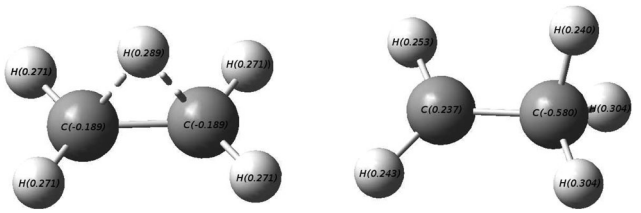

(a)bridged (b)classical

Fig. 1 Panel (a) represents the minimum energy ''bridged'' structure for $C_2H_5^+$, whereas panel (b) shows the ''classical'' structure that is a transition state in most levels of electronic structure theory. The figures also demonstrate the relative asymmetry of charge. The ''classical'' structure is approximately 6 kcal mol^{-1} higher in energy as compared to the ''bridged'' structure (see Table 1).

In this publication, we consider the carbocations $C_2H_5^+$ and $C_3H_3^+$, and a few stable conformations for these molecules are presented in Fig. 1 and 2. In $C_2H_5^+$, the ''classical'' structure (Fig. 1(b)) is a transition state under all levels of electronic structure theory and hence is generally not expected to contribute to spectra. However, as we will see here, vibrational signatures unique to this ''classical'' configuration do appear in the computed spectra from *ab initio* dynamics when initial conditions are chosen so as to include sufficient energy to represent zero-point vibrations corresponding to the initial structure. These results are also confirmed by studying quantum nuclear contributions from reduced dimensional studies. Our results here provide an alternative interpretation to the recent argon-tagged action spectroscopy results on this species.[17,18] The $C_3H_3^+$ system, on the other hand, is characterized by a high-degree of permutational exchange amongst the hydrogen and the carbon atoms. This leads to complex vibrational spectral behavior that has contributions from several structures. In fact we find deep similarities between the conformational migration in $C_2H_5^+$ and $C_3H_3^+$ and that already noted for $C_2H_3^+$ in ref. 32. We discuss mechanistic aspects of configurational change in Section III. In Section IIIA, the reduced dimensional distributions, associated potential surfaces, and the resulting quantum nuclear eigenstates are presented. In Section IV we present the resulting vibrational properties, and the structural transformations are further probed using two-dimensional time–frequency analysis. The AIMD simulations used here are computationally intensive, and the study utilizes several million electronic structure calculations. In Section II, we present a careful investigation of the isomer stabilization energy for $C_2H_5^+$ and $C_3H_3^+$ using DFT (M062X and B3LYP exchange–correlation functionals), MP2, MP4 and CCSD(T) to arrive at the best compromise between accuracy and efficiency. The choice (M062X and B3LYP) allows us to perform several AIMD simulations under a variety of initial conditions. Conclusions from our study are provided in Section V.

II. Choice of electronic structure theory

Tables 1 and 2 provide a summary of the relative stability of the two most stable geometries for $C_2H_5^+$ and $C_3H_3^+$, respectively. The data includes calculations performed here and those by others.[1,16,21,35–38]

Given our goals to compute relatively long *ab initio* dynamics trajectories that included all levels of anharmonicity, our choice of electronic structure theory was based on both accuracy and efficiency. For example, the study here includes a total of 59 AIMD simulations, each simulation being roughly 5–10 ps in length. Given an average time step of 0.1 fs, to help conserve the overall system Hamiltonian within the sub-kcal mol^{-1} range, this amounts to a few million electronic structure calculations, which is clearly prohibitive even for this small a system when coupled cluster accuracy at the large basis limit is desired. [This situation is likely to change in the near future with the advent of new methods, such as the fragment based *ab initio* molecular dynamics method,[39–41] that do provide MP2 and coupled cluster accuracy at significantly reduced computational cost.] At this time, however, a compromise must be made between accuracy and computational cost.

As can be seen in Table 1, for $C_2H_5^+$, the difference in energy between the lower-energy ''bridged'' structure and the higher-energy ''classical'' structure ranges from 3.5 to 9.3 kcal mol^{-1} depending on level of theory and basis set. [Note that the so-called ''classical'' structure was found to be a transition state at all levels of theory probed.] By comparing the results obtained for the computationally ''cheaper'' M062X, B3LYP,

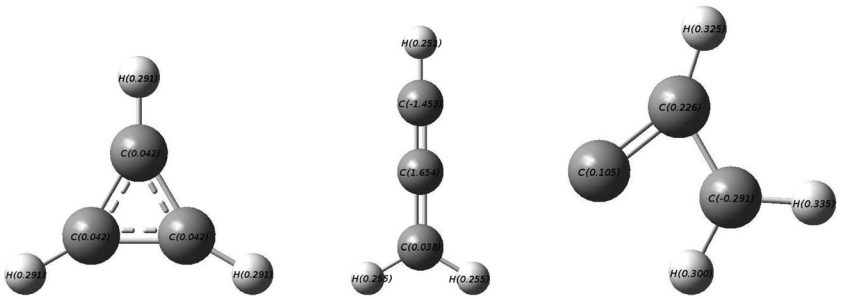

(a)cyclic (b)straight (c)prop-2-en-1-yl-3-ylidine

Fig. 2 Stable structures for $C_3H_3^+$. While the ''cyclic'' structure is nearly 30 kcal mol^{-1} lower in energy as compared to the ''straight'' structure, the zero-point energy in the ''cyclic''-well is roughly of the same order. Energetic stabilization is shown in Table 2. The ''prop-2-en-1-yl-3-ylidine'' structure is approximately 70 kcal mol^{-1} higher in energy relative to the ''cyclic'' structure.

 This journal is © the Owner Societies 2017

Published on 06 September 2017. Downloaded by Indiana University Libraries on 7/27/2018 11:48:17 AM.

Table 1 Differences in equilibrium geometry, relative energies, and vibrational zero point energies for the "bridged" and "classical" structures for $C_2H_5^+$, at different levels of electronic structure theory

Level of theory	Bridged[a] (Å)	Classical[a] (Å)	ΔE^b (kcal mol^{-1})	$ZPE_{bridged}$ (kcal mol^{-1})	$ZPE_{classical}$ (kcal mol^{-1})	ΔE_{ZPE} (kcal mol^{-1})
M062X/6-311++G**	0.00	0.00	5.9	38.4	37.5	6.8
M062X/6-31+G(d,p)	0.06	0.07	5.5	38.6	37.7	6.4
M062X/aug-cc-pvtz	0.08	0.09	6.0	38.4	37.5	6.9
B3LYP/6-311++G**	0.10	0.10	3.7	37.8	37.1	4.4
B3LYP/6-31+G(d,p)	0.15	0.16	3.5	38.0	37.3	4.2
MP2/6-311++G**	0.06	0.06	7.9	38.7	37.8	8.8
MP2/6-31+G(d,p)	0.11	0.10	7.5	39.5	38.5	8.5
MP4/6-311++G**//M062X/6-311++G**			7.0			
MP4/6-31+G(d,p)//M062X/6-311++G**			6.6			
MP4/aug-cc-pvtz//M062X/6-311++G**			7.3			
CCSD(T)/6-311++G**//M062X/6-311++G**			6.5			
CCSD(T)/6-31+g(d,p)//M062X/6-311++G**			6.2			
CCSD(T)/aug-cc-pvdz//M062X/6-311++G**			6.3			
B3LYP/6-311+G(d,p)[c]			3.7			
MP2/6-311+G(3df,2p)//B3LYP/6-311+G(d,p)[c]			8.4			
MP3/6-311+G(3df,2p)//B3LYP/6-311+G(d,p)[c]			7.3			
MP4D/6-311+G(3df,2p)//B3LYP/6-311+G(d,p)[c]			7.3			
MP4DQ/6-311+G(3df,2p)//B3LYP/6-311+G(d,p)[c]			7.0			
MP4SDQ/6-311+G(3df,2p)//B3LYP/6-311+G(d,p)[c]			6.8			
MP4SDTQ/6-311+G(3df,2p)//B3LYP/6-311+G(d,p)[c]			7.5			
CCSD/6-311+G(3df,2p)//B3LYP/6-311+G(d,p)[c]			6.4			
CCSD(T)/6-311+G(3df,2p)//B3LYP/6-311+G(d,p)[c]			6.9			
MP2(v)[d]			8.0			
MP2-R12(v)[d]			9.3			
MP4SDQ-FC/6-31G(d)[c]			4.7			
CCSD(T)/aug-cc-pVTZ[e]	0.11	0.57	7.2			

[a] Mean absolute deviation in the distance matrix calculated with reference to M062X/6-311++G**. [b] Energetic stabilization of the "bridged" configuration with reference to the "classical" configuration. [c] From Table 2.2 in ref. 1. [d] From ref. 21: Only valence MO contributions. Basis set for carbon: [9s,5p,1d/5s,4p,1d]. Hydrogen: [5s1p/3s1p]. [e] Ref. 35: Coupled cluster and MBPT methods are used to determine NMR shifts, including predictions of coupling constants.

Table 2 Differences in equilibrium geometry, relative energies, and vibrational zero point energies for the most important isomers shown in Fig. 2 for $C_3H_3^+$, at different levels of electronic structure theory

Level of theory	Cyclic[a] (Å)	Straight[a] (Å)	ΔE^b (kcal mol^{-1})	ZPE_{cyclic} (kcal mol^{-1})	$ZPE_{straight}$ (kcal mol^{-1})	ΔE_{ZPE} (kcal mol^{-1})
M062X/6-311++G**	0.00	0.00	34.3	28.5	27.0	35.8
M062X/6-31+G(d,p)	0.05	0.11	35.3	28.6	27.1	36.8
M062X/aug-cc-pvtz	0.09	0.07	35.1	28.5	26.9	36.7
B3LYP/6-311++G**	0.02	0.04	25.3	28.3	26.8	26.8
B3LYP/6-31+G(d,p)	0.10	0.15	26.4	28.3	26.9	27.8
MP2/6-311++G**	0.15	0.20	31.5	28.5	27.2	32.8
MP2/6-31+G(d,p)	0.10	0.22	32.6	28.8	27.4	34.0
MP4/6-311++G**//M062X/6-311++G**			27.5			
MP4/6-31+G(d,p)//M062X/6-311++G**			28.5			
MP4/aug-cc-pvtz//M062X/6-311++G**			28.2			
CCSD(T)/6-311++G**//M062X/6-311++G**			29.5			
CCSD(T)/6-31+G(d,p)//M062X/6-311++G**			30.5			
CCSD(T)/aug-cc-pvdz//M062X/6-311++G**			29.5			
MP2/6-311G**//MP2/6-31G*[c]			31.6			
MP4/6-311G(2d,2p)//MP2/6-31G*[c]			26.1			
CCSD(T)/cc-pVTZ[d]			23.4			
CCSD(T)/cc-pV(T,Q,5Z)[e]	0.16	0.08	27.9			
Experimental[f]			25			

[a] Mean absolute deviation in the distance matrix calculated with reference to M062X/6-311++G**. [b] Energetic difference between the "cyclic" and "straight" configurations. [c] From ref. 36, which supplies further calculations not reported here. [d] Ref. 16: Calculations used to support experimental spectra obtained *via* rare gas-tagging infrared laser photodissociation spectroscopy. [e] Ref. 37: Geometry optimizations include core-correlation correction and scalar-relativistic correction and were used to calculate quartic force fields. [f] Ref. 38: Energy-resolved electron beams were used to determine appearance potentials and hence relative stability. See ref. 38 for additional details.

and MP2 levels of theory, with appropriate higher level calculations, it can be seen that as is the case for $C_2H_3^+$ in ref. 32, for the case of $C_2H_5^+$, B3LYP underestimates the stability of the "bridged" structure, whereas MP2 slightly over-estimates it.

Published on 06 September 2017. Downloaded by Indiana University Libraries on 7/27/2018 11:48:17 AM.

Thus, for this system, M062X provides the best compromise between accuracy and computational efficiency. As a result, we employed dynamical simulations constructed using the M062X[42] functional with the 6-311++G** Gaussian basis set for our analysis of $C_2H_5^+$.

For $C_3H_3^+$, as shown in Table 2, the ''cyclic'' structure was seen to be stabilized by 23–35 kcal mol^{-1} relative to the ''straight'' structure depending on the level of theory and basis set. This system, however, differs from both $C_2H_5^+$ and $C_2H_3^+$ in terms of the optimal, less-expensive level of theory. In this instance, both MP2 and M062X overestimate the stability of the ''cyclic'' structure in comparison to higher level calculations and the experimentally determined value. B3LYP was seen to provide the best compromise between accuracy and efficiency. However, to maintain consistency with the studies performed on $C_2H_5^+$ and $C_2H_3^+$, simulations using the M062X[42] functional with the 6-311++G** Gaussian basis set were analyzed in addition to calculations constructed using the B3LYP[43] functional with the 6-311++G** Gaussian basis set.

In total, 33 M062X simulations and 26 B3LYP simulations were constructed spanning a wide range of input kinetic energies, for the two different systems investigated. The total simulation time in each case ranged between 5 and 10 picoseconds which allowed the system to sample a wide range of the available configurational space. Further details regarding the *ab initio* molecular dynamics simulations constructed in this publication, including simulation time, survey of kinetic energy and potential energy, the conservation of total energy, and relative population analysis, can be found in ESI.† As such, computed spectra are direct functions of the subspace of the global potential surface sampled. As a result, sampling-energy dependent properties were also probed in our studies. In this regard, the choice of initial conditions is particularly important to clarify since this choice determines the phase-space structural distribution function. Based on previous AIMD studies on a wide-range of hydrogen bonded systems, it is known that the argon-tagged action spectra are recorded using low temperature ions, and hence, low temperature and low energy AIMD trajectories (*i.e.*, trajectories with low input kinetic energies) are in good agreement with these results[44–48] for strong hydrogen bonded systems. In the case of simulations that model infrared multiple photon dissociation (IRMPD) effectively,[49–55] larger energies[46,56] are required. While a range of energies were studied for the problems discussed here, the presented data in this publication are from trajectories within a range of total energies that include the harmonic zero-point energy. This allowed us to probe the full potential surface in a systematic fashion, and properties are computed as a function of these sampling conditions. Data and trends from additional trajectories can be found in ESI.†

III. Proton shuttles and CH-group transmutation during dynamics

In many of our higher energy AIMD simulations, the structures of $C_2H_5^+$ and $C_3H_3^+$ are highly fluxional. Before undertaking the discussion on how the fluxionality of each system was quantified, a brief discussion on the qualitative mechanisms by which the interconversion of geometries occurs is conducted.

The configurational migration processes of $C_2H_5^+$ and $C_3H_3^+$ are best understood when considered together with the previously observed[32] proton shuttle in $C_2H_3^+$. (To supplement this discussion, the $C_2H_3^+$ proton shuttle mechanism is presented here in Fig. 3(a) along with those found in this study for $C_2H_5^+$ and $C_3H_3^+$ in Fig. 3(b) and (c), respectively.) In the case of $C_2H_3^+$, the bridge proton performs large amplitude excursions along a plane that is parallel to the carbon–carbon bond. This is on account of the relatively flat potential energy surface experienced by the bridge proton along this direction. When the energy of the system is increased further, the large amplitude excursions performed by the bridge proton begin to overlap with the domain of oscillations of the CH protons in $C_2H_3^+$ and eventually the bridge proton permutes its position with one of the CH protons. This process is pictorially depicted in Fig. 3(a) and is facilitated by the fact that the ground state corresponding to motion along the aforementioned direction is above the barrier that separates the ''bridged'' and ''classical'' conformations in $C_2H_3^+$. While the mechanism by which the bridge proton of $C_2H_5^+$ permutes its position with the CH_2 protons is a relatively straightforward analogue of the mechanism outlined for $C_2H_3^+$—as can be noted in Fig. 3(b)—a much more complex phenomenon is observed for $C_3H_3^+$.

The analysis of the fluxionality of $C_3H_3^+$ was simplified upon noting that the ''bridged'' configuration in $C_2H_3^+$ is quite similar to the ''cyclic'' configuration in $C_3H_3^+$, when the axial CH-group in the latter is identified as a single unit and hence takes the place of the bridge proton in $C_2H_3^+$. This isomorphism is emphasized by denoting $C_3H_3^+$ as $C_2H_2A^+$, where A is the CH-group and is marked in Fig. 3(c) using ellipses. Indeed we find during our higher energy simulations that this CH-group can migrate, much like the bridge proton does in $C_2H_3^+$, towards one of the side carbons and exchange spots with the hydrogen. However, such a large scale oscillation by the bulky CH-group leads to a significant angular momentum penalty on the system that needs to be compensated by a torque on the carbon skeleton in the opposite direction. A second pathway that does not have this angular momentum penalty appears to be preferred in our simulations as indicated in Fig. 3(c). Here, the axial CH group tilts and instead of the entire CH group migrating towards one of the carbons (as would be the case for $C_2H_3^+$), the CH-bond cleaves to allow hydrogen and carbon atoms to migrate in opposite directions as shown in Fig. 3(c). This leads to the appearance of the ''straight'' configuration for $C_3H_3^+$ during our higher temperature simulations. A reverse of this mechanism was also observed when $C_3H_3^+$ converted from its ''straight'' to ''cyclic'' form. The corresponding distribution of nuclei is shown in Fig. 4.

Given that the total angular momentum is conserved in all our simulations, the migration and transmutation of the CH group needs to be compensated by an equivalent angular displacement of the carbon–carbon bond axis in the opposite direction, making the CH migration even more likely. Given the

 This journal is © the Owner Societies 2017

Published on 06 September 2017. Downloaded by Indiana University Libraries on 7/27/2018 11:48:17 AM.

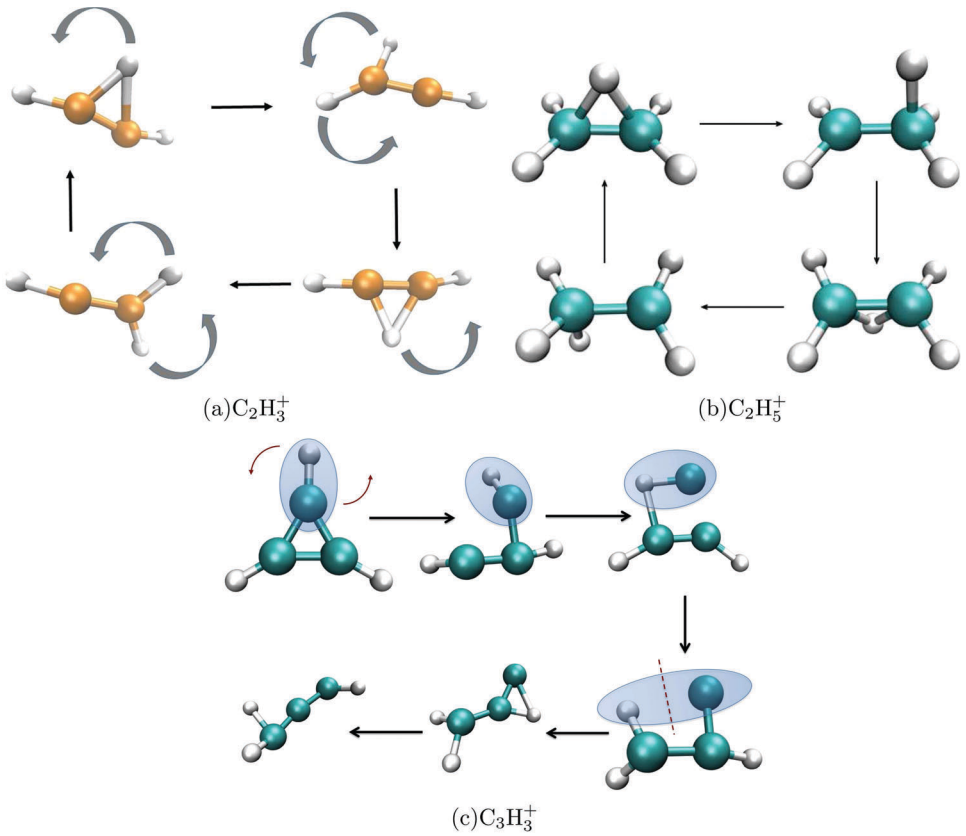

Fig. 3 Highlight of the conformational transformation mechanisms for $C_2H_3^+$, $C_2H_5^+$ and $C_3H_3^+$. The associated nuclear distribution functions are given in Fig. 5(b) and 7(b).

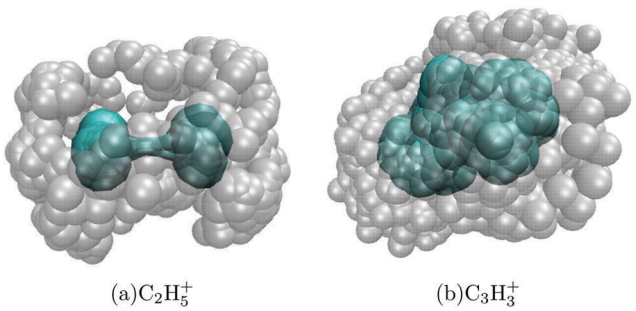

Fig. 4 Depiction of the fluxional nature of $C_2H_5^+$ and $C_3H_3^+$ during high energy AIMD simulations. The figures reveal the distribution of all hydrogen nuclei (gray) surrounding the central carbon atoms (aquamarine). The distributions, which have not been symmetrized, were obtained from the AIMD trajectories described in the ESI.†

larger mass of the migrating CH group (as compared to the migrating bridge proton in $C_2H_3^+$), angular momentum can only be conserved if the carbon–carbon bond axis is tilted to a much larger extent in the opposite direction (as compared to the corresponding case for $C_2H_3^+$), which partially ensures the almost spherical distribution of carbon and hydrogen atoms in Fig. 4(b).

As ref. 57 demonstrates, it may be possible to use circularly polarized light to detect the "bridged" to "classical" isomeric transformation for $C_2H_3^+$. It would be of interest to determine if similar methodology could be used to track the interconversion of geometries for our two systems.

A. Reduced dimensional potentials, classical and quantum nuclear distributions

To probe the extent of conformational flexibility, we invoke a reduced representation of the transfer process. To this end, conformational transfer coordinates were independently defined for $C_2H_5^+$ and $C_3H_3^+$. These coordinates were then employed to construct low-dimensional distributions for geometries and compute reduced dimensional potential surfaces. The potential surfaces were, in turn, utilized to obtain reduced dimensional eigenstates to elucidate quantum nuclear effects. Each of the aforementioned items for both $C_2H_5^+$ and $C_3H_3^+$ is given in Sections IIIA 1 and IIIA 2.

1. $C_2H_5^+$. For the case of $C_2H_5^+$, θ, the reduced dimensional coordinate, represents the angle made by the most "bridge-like" hydrogen and the axis defined by the line joining the centers of masses of the two hydrogens of each CH_2 group. The most "bridge-like" proton is established by the merit of being excluded from each CH_2 moiety, *i.e.* there are two other protons closer to the carbon atom of each moiety. A pictorial illustration is provided in Fig. 5(a). Additionally, as the "bridge" proton orbits around the CH_2–CH_2 framework, it performs a proton-relay. This kind of permutation is reminiscent of the Grotthuss mechanism[34] as was noted earlier in ref. 32 and causes another

Published on 06 September 2017. Downloaded by Indiana University Libraries on 7/27/2018 11:48:17 AM.

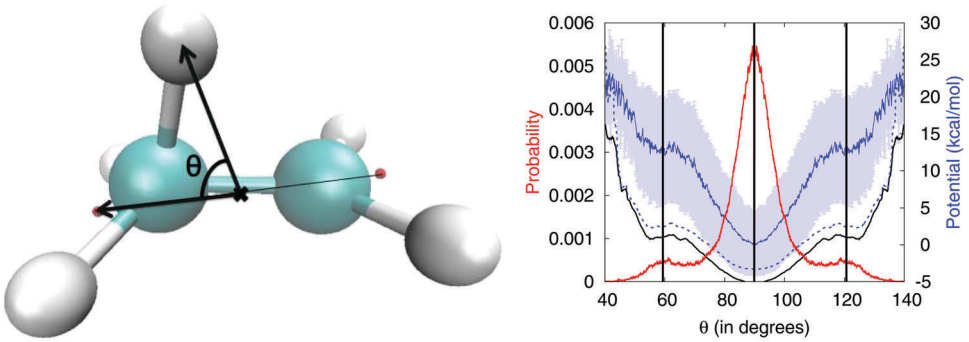

(a)Reduced Dimensional Coordinate (b)Distribution and Potential

Fig. 5 Panel (a) defines the reduced dimension shown along the horizontal axis in panel (b), which indicates the distribution of geometries in the classical AIMD simulations (red), the infinite temperature potential (blue), the smoothed, 500 K potential (dashes), and the smoothed, zero Kelvin potential (black). Eqn (1), which includes the temperature-dependent term β, describes how reduced dimensional potentials are computed. Also see Appendix A. Note that panel (b) is permutationally symmetrized to facilitate the accurate determination of eigenvalues.

proton to become the most "bridge-like" proton. There exists a symmetry in the potential experienced by the effective nuclear coordinate, θ, as seen from the reduced dimensional potential shown in Fig. 5(b). To clarify, the black and blue curves in Fig. 5(b) represent reduced dimensional potentials that include thermally sampled contributions from orthogonal degrees of freedom according to

$$\frac{1}{Q}\int \mathrm{d}\theta^{\perp} \exp[-\beta H] V(q) = \tilde{V}_{\beta}(\theta), \qquad (1)$$

where the quantity "q" includes all degrees of freedom in the system, β is the inverse temperature ($\beta = 1/kT$), $\theta^{\perp}$ denotes all degrees of freedom orthogonal to θ and the denominator Q is the system partition function. We emphasize that $V(q) \equiv V(\theta;\theta^{\perp})$. Thus the potential surface generated here is a thermally weighted "effective" surface for the interconversion of geometries, that receives an average (thermalized) interaction from the motion of degrees of freedom orthogonal to θ (denoted by $\theta^{\perp}$) and the associated electronic structure change. A brief discussion of the underlying approximations in eqn (1) is provided in Appendix A.

Such potential surfaces, along with associated classical distribution, are represented in Fig. 5(b), one using a zero Kelvin canonical sampling in eqn (1) (black) and the other using an infinite Kelvin canonical sampling (blue). In addition, for illustrative purposes, we have provided an intermediate temperature potential at 500 K. Standard deviations due to statistics along degrees of freedom orthogonal to θ are shown in gray. Critically, as the orthogonal sampling temperature in eqn (1) increases, the barrier height between the "bridged" and "classical" configurations also increases due to the greater entropy that is deposited onto the modes that are orthogonal to the transfer coordinate. It is clear from these potential surfaces that the zero Kelvin barrier between the "bridged" configuration (90 degrees) and the "classical" transition state (60 degrees) is approximately 5 kcal mol^{-1} and the infinite temperature barrier is roughly 15 kcal mol^{-1} for $C_2H_5^+$.

Note that a direct fit of the symmetrized potential necessitated a polynomial of at least order 10 along the reduced dimensional coordinate; yet, this still does not capture some of the anharmonicity near the "classical" shoulders of the potential well. It is critical to note that the methodology used here samples the full anharmonicity of the potential with the configurational space sampled based on simulation energy. Additionally, as will be enumerated in Section IV, a non-perturbative methodology is used to obtain computed spectra presented in this work. While methodologies that treat anharmonicity as a perturbative correction are clearly restricted for strongly anharmonic systems, our non-perturbative method has demonstrated generality and effectiveness.[44–48,56,58,59]

We next solve the one-dimensional nuclear Schrödinger equation for the degree of freedom, θ, and potential shown in Fig. 5(b), with the kinetic energy operator represented using "Distributed Approximating Functionals" (DAFs)[32,60–63] (see the ESI†). The eigenstate density for the first eigenstate of $C_2H_5^+$ is shown in Fig. 6, with the eigenvalue stated in the figure caption. As may be noted from Fig. 6(a), the ground state of $C_2H_5^+$ has significant density in the "classical" configuration. Thus, one could expect the classical structure to be populated at ambient temperatures. As we will see in Section IV, this has critical significance in the vibrational spectrum of the system, which shows contributions from the classical structure, despite it not being a minimum energy stable structure!

2. $C_3H_3^+$. For the case of $C_3H_3^+$, conformational transitions are studied through introduction of the reduced dimensional angle shown in Fig. 7(a). Specifically, the angle subtended by each peripheral carbon atom on the center of the remaining two carbon atoms is computed, and the maximum angle from the aforementioned set is used to depict conformational transitions. This angle is denoted by θ_{max} in Fig. 7(a) in all related discussion. Yet again, we observe a symmetry due to permutation of the carbon and hydrogen atoms that results in the potential given in Fig. 7(c), where we emphasize the pertinent range of angles for individual carbon atoms by separating the range of the horizontal axis with vertical bars. Extending this analysis to the hydrogen atoms in $C_3H_3^+$ that also cyclically permute positions, one obtains a two-dimensional

 This journal is © the Owner Societies 2017

Published on 06 September 2017. Downloaded by Indiana University Libraries on 7/27/2018 11:48:17 AM.

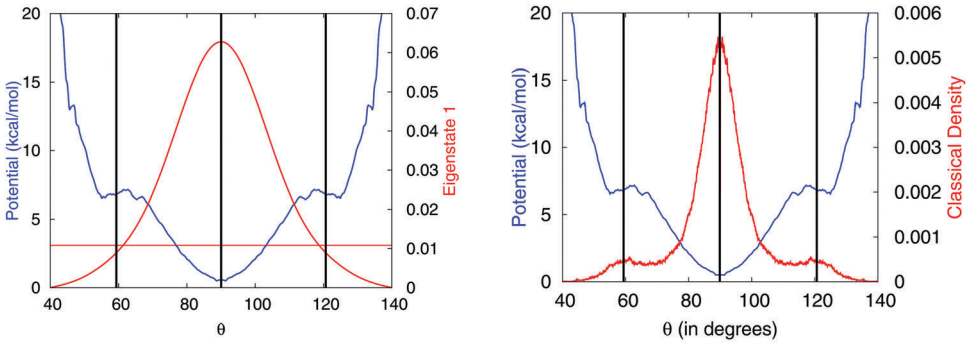

(a)M062X (3.096 kcal/mol) (b)Classical Distribution

Fig. 6 In panel (a), the first eigenstate along the θ reduced dimensional direction for $C_2H_5^+$ is shown in red with the zero Kelvin permutationally symmetrized potential in blue. The horizontal red line corresponds to the eigenvalue. For comparison, in panel (b), we have reproduced the classical AIMD structural distribution used to compute the potential surfaces for the quantum nuclear description.

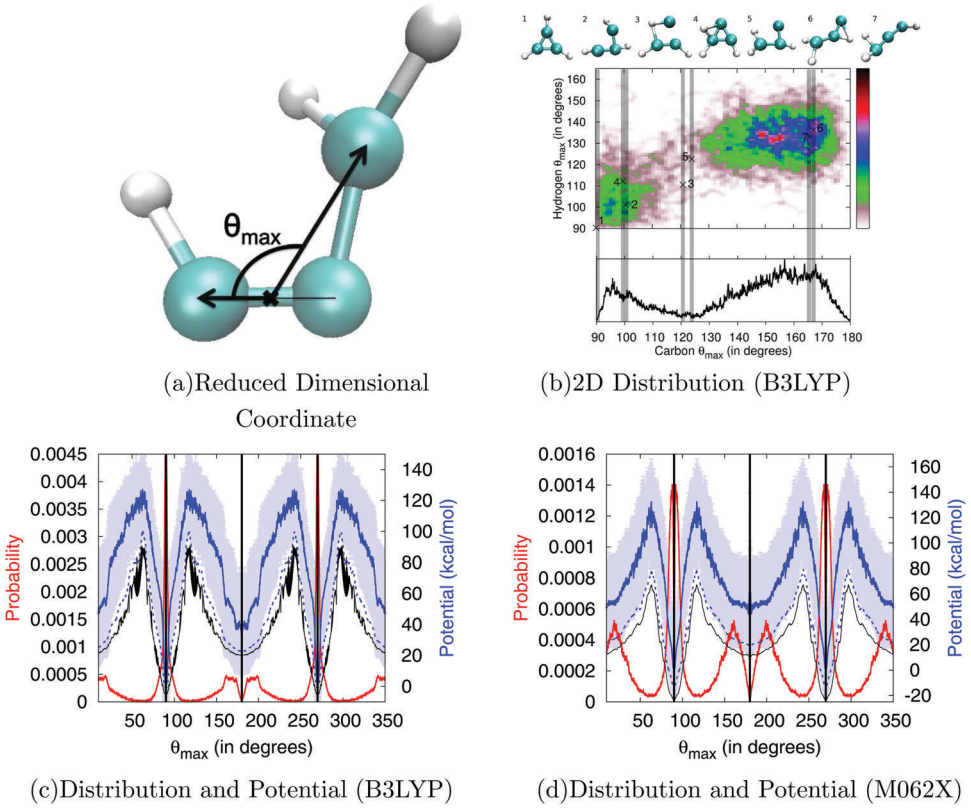

(a)Reduced Dimensional Coordinate (b)2D Distribution (B3LYP)

(c)Distribution and Potential (B3LYP) (d)Distribution and Potential (M062X)

Fig. 7 Panel (a) defines the reduced dimension shown along the horizontal axes of panels (b–d). In panel (b), the two-dimensional classical distribution also includes an angle analogous to θ_{max} but defined for the hydrogens and used as the vertical axis. Panel (b) shows the greater significance of the carbon angle in depicting conformation transitions. Panels (c and d) show the distribution of geometries in the classical AIMD simulations (red), the infinite temperature potential (blue), the smoothed, 4000 K potential (dashes), and the smoothed, zero Kelvin potential (black). The potentials are computed as given in eqn (1). Also see discussion in Appendix A.

representation of conformational transition that is depicted in Fig. 7(b). The top panel of Fig. 7(b) also shows representative nuclear geometries at different maximum carbon angles, and it is apparent from these figures how the prop-2-en-1-yl-3-ylidine configuration (Fig. 2(c)) may be visited during the transition from "cyclic" to "straight", with the corresponding populations obtained from AIMD, shown in Fig. 7(b). There are obviously multiple pathways connecting the two critical regions shown in the two-dimensional distribution in Fig. 7(b), and an approximate pathway is provided through the structures on the top panel; these structures are also correlated with the mechanistic discussions at the top of Section III. However, from Fig. 7(b), it is also apparent that the dependence on the carbon angle during the transfer process is much more significant, and, hence, this is the

Published on 06 September 2017. Downloaded by Indiana University Libraries on 7/27/2018 11:48:17 AM.

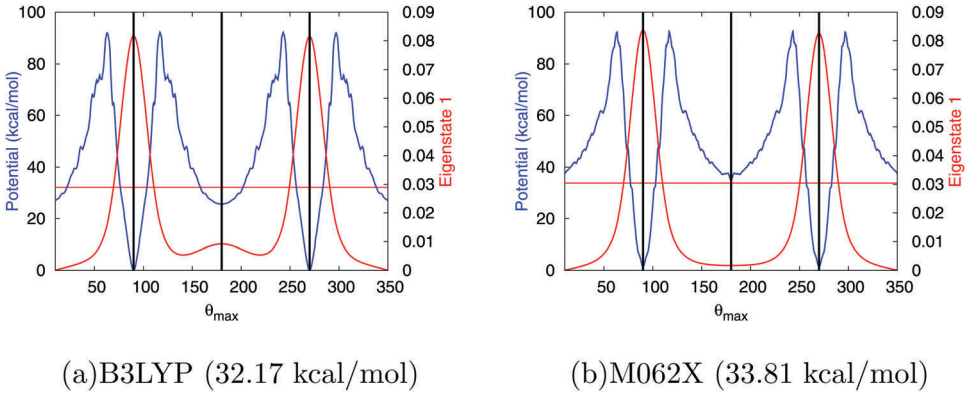

Fig. 8 Ground eigenstates as a function of θ_{max} for $C_3H_3^+$ are shown in red with the zero Kelvin permutationally symmetrized potential in blue. The horizontal red line corresponds to the respective eigenvalues, which are given in the figure caption along with the level of theory.

angle followed for analysis of reduced-dimensional potential and quantum-nuclear eigenstates.

As in the case of $C_2H_5^+$, we proceed to analyze the potential experienced along the chosen reduced dimensional carbon angle coordinate using eqn (1) (where θ is now replaced by θ_{max}), and the corresponding first eigenstate is shown in Fig. 8 for both the B3LYP and M062X potential surfaces. From these, the 0 K barrier between the "cyclic" (90 degrees) and "straight" (180 degrees) structures is approximately 90 kcal mol^{-1} from the "cyclic" potential well and approximately 60 kcal mol^{-1} from the "straight" well (which agrees well with previous estimates for this value[16]). As for the case of $C_2H_5^+$, here again the potential is highly anharmonic.

However, upon obtaining the reduced dimensional eigenstates, we find a significant difference between the lowest energy eigenstates depending on the level of theory. While the ground state for M062X shows no density in the potential well corresponding to the "straight" configuration, the B3LYP ground state shows population greater than 10% of the corresponding population in the cyclic configuration. This is due to the fact that the zero point energy for the case of B3LYP is sufficiently high to overcome the energetic difference between the "cyclic" and "straight" configuration wells. Furthermore, as already noted in Table 2, given the closer agreement between the isomer energetic differences for B3LYP as compared to CCSD(T),[16,37] MP4,[36] and experiment,[38] we expect the subtle difference between the B3LYP ground eigenstates to have a critical impact on the discussion of vibrational spectra.

IV. Vibrational properties of the anomalous carbocations computed from dynamics

The discussion thus far has been restricted to the analysis of the potential surface sampled along the transfer coordinates using AIMD simulations at a variety of energies. These surfaces have allowed us to conclude that (i) in the case of $C_2H_5^+$, the "classical" structure—despite being a transition state—has a significant contribution to the zero-point eigenstate, and (ii) in the case of $C_3H_3^+$, the "straight" configuration may be populated depending on the level of electronic structure theory that is used. However, since the B3LYP conformational energies better correspond to higher level and experimental values (see Table 2), our analysis here will mainly be based on that surface. In this section, we utilize a selected set of AIMD simulations to compute dynamically averaged vibrational properties and compare these with experimental vibrational action spectra.[15–18] More details are given in ESI.†

A. A brief description of the experimental argon-tagged action spectroscopy results and analysis of the corresponding harmonic spectral results

To introduce the challenges involved here, we present in Fig. 9 the experimental spectra for $C_2H_5^+$ and $C_3H_3^+$ along with the corresponding harmonic features. (See ESI† for a description of how the harmonic modes in the "classical" isomer for $C_2H_5^+$ may be thought to arise from a linear combination of those from the "bridged" structure.) Clearly, it appears that multiple conformations may contribute to the experimental results obtained through argon-tagged action spectroscopy.[16,17] Note that in the experimental methodology discussed in ref. 16 and 17, $C_2H_5^+$ and $C_3H_3^+$ ions were created *via* pulse discharge/supersonic expansion from their respective precursors. Although specific details can be found in ref. 16 and 17, two important experimental considerations follow.

- The authors in ref. 17 explain the appearance of certain unexpected experimental peaks (shown using blue asterisks in Fig. 9(a)) as being due to an $H^+N_2Ar_2$ impurity in the $C_2H_5^+$ spectrum. Based on our analysis in the previous section of Fig. 6, the ground eigenstate does show population in the "classical" configuration. Indeed, as we will see in Section IV B 1, our finite temperature AIMD trajectories recover these smaller features in the $C_2H_5^+$ spectrum. We have also computed AIMD trajectories for $H^+N_2Ar_2$, and these are presented in the ESI.† While it appears that indeed this impurity can contribute to the spectrum as noted in ref. 17, our results here will show that the appearance of the classical structure is another, more plausible, rationale.

 This journal is © the Owner Societies 2017

Published on 06 September 2017. Downloaded by Indiana University Libraries on 7/27/2018 11:48:17 AM.

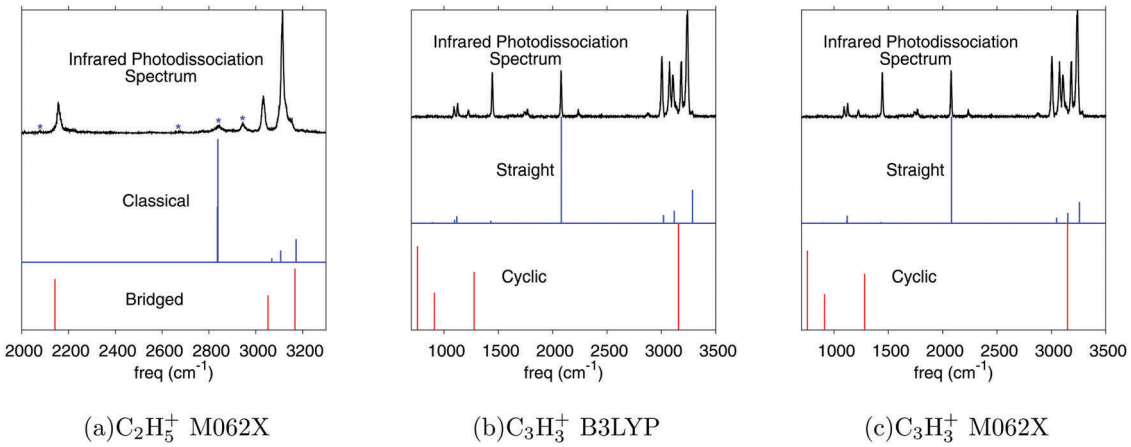

(a)$C_2H_5^+$ M062X (b)$C_3H_3^+$ B3LYP (c)$C_3H_3^+$ M062X

Fig. 9 The experimental spectra for (a) $C_2H_5^+$ and (b and c) $C_3H_3^+$ along with the corresponding harmonic fundamentals. Harmonic frequencies are scaled by 0.972 for M062X and 0.975 for B3LYP. The asterisks in panel (a) denote peaks attributed to an impurity, $H^+N_2Ar_2$, in ref. 17.

- In the case of $C_3H_3^+$, the precursor for determination of experimental spectra in ref. 16 is propargyl bromide, and a large energetic barrier (approximately 49 kcal mol^{-1} [64]) inhibits interconversion of this "straight-like" isomer into the more-stable "cyclic" isomer. Thus, although variation of the ion source conditions altered the ratio of "straight" to "cyclic" features observed in the various spectra, the higher-energy "straight" configuration dominated spectral results at energies sufficiently low to maintain the argon tag required for this spectroscopic methodology due to insufficient energy supplied for the "straight" precursor to overcome the aforestated isomerization barrier.[16] Therefore, AIMD spectra presented in this publication focus on simulations where the "straight" isomer was the starting configuration. In addition, while it is postulated in ref. 16 that the "cyclic" contribution may be produced by means of plasma chemistry (and not through isomeric interconversion), as is already clear from Fig. 10, the relevant eigenstate—the lowest-energy eigenstate with the "straight" well being primarily populated—of $C_3H_3^+$ does demonstrate some contribution from the "cyclic" isomer. Indeed, in Section IV B 2, we find that our dynamically averaged AIMD spectra provide a reasonable interpretation of the experimental results.

B. Vibrational spectra from AIMD simulations

The harmonic approximation utilized for reference in the previous subsection is a sensible estimate for rigid covalent systems; however, it is not effective for highly fluxional, anharmonic systems[44,46–48,56,58,59] such as those studied here. These fluxional systems demonstrate a high level of anharmonicity as evinced by the reduced potential surfaces shown in Fig. 5(b), 7(c) and (d). (The minimum polynomial order required to capture the anharmonicity in these figures is sixth-order for $C_2H_5^+$ and fifth-order for $C_3H_3^+$. But the resultant polynomials lack permutational symmetry. Requiring the polynomial fits to obey permutational symmetry necessitates a larger order fit, as noted above.) Additionally, previous work[46,47,56] suggests that spectra for highly anharmonic systems may be dominated by how the harmonic modes couple to produce new modes due to the anharmonicity. Hence, a computational methodology to compute vibrational spectra with all degrees of anharmonicity for these fluxional carbocations is desired. Vibrational second

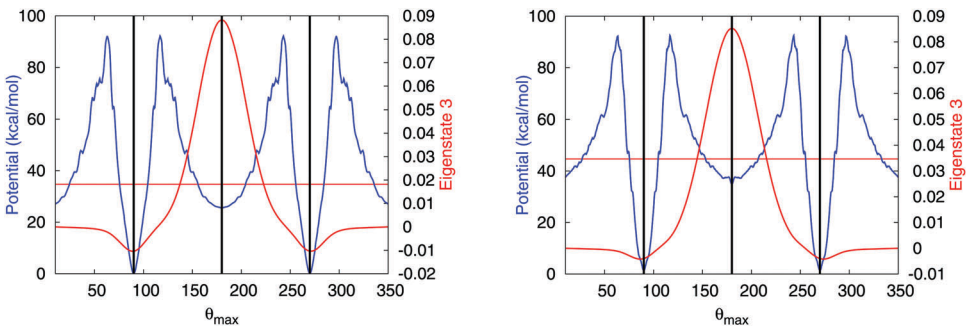

(a)B3LYP (34.7374 kcal/mol) (b)M062X (44.667 kcal/mol)

Fig. 10 The third eigenstate along θ_{max} $C_3H_3^+$ (red) and the zero Kelvin permutationally symmetrized potential (blue). The horizontal red line corresponds to the respective eigenvalues, which are given in the figure caption along with the level of theory. (The ground eigenstate is shown in Fig. 8. The symmetry of the potential allows the second eigenstate distribution to differ from the ground eigenstate through the presence of a node at the center of symmetry of the potential.)

Published on 06 September 2017. Downloaded by Indiana University Libraries on 7/27/2018 11:48:17 AM.

order perturbation theory (VPT2)[65–68] and vibrational configuration interaction theory (VCI)[65–68] have previously been used on anharmonic systems.[37,69,70] These methodologies are a step up from the harmonic approximation in that they account for some degree of anharmonicity of the potential. Yet, VPT2 generally involves a harmonic reference that is perturbatively corrected with potentials up to fourth order, and the VSCF method has been found to be insufficient in the study of highly anharmonic systems.[71] Hence, these methods may have difficulty in systems such as those presented here. The VCI method would in principle accurately represent these problems, but computational challenges remain.

Here, we compute vibrational spectra from our AIMD simulations. The simulation kinetic energy in a classical AIMD treatment gradually tunes in anharmonicity by varying the range of the potential surface sampled. We simulate the vibrational spectra by computing the one-dimensional Fourier Transforms for the Dipole–Dipole Auto-correlation Function obtained from the dynamics trajectories. The expressions are presented in ESI.† We additionally compute the two-dimensional Fourier Transforms of the Dipole–Dipole Auto-correlation Function to probe conformational transitions. Note that $\alpha_{\mu}^{QC}(\omega)$ in eqn (B2) in Appendix B has been shown to accurately reproduce vibrational properties in agreement with vibrational action spectroscopy experiments.[44–47,56] Furthermore, these kinds of studies have been used to understand the differences between experimental techniques,[46,56] in particular, infra-red multiple photon dissociation (IRMPD)[53–55,72,73] and argon tagged action spectroscopy.[74,75]

Selected vibrational spectra for $C_2H_5^+$ and $C_3H_3^+$ are presented in Sections IV B 1 and IV B 2. The average total energies for these trajectories are noted, and the harmonic fundamentals are presented in the bottom panel for each cascade plot. Note that all spectra computed using M062X and B3LYP have their frequencies scaled by 0.972 and 0.975 respectively to account for the fact that the AIMD simulations here do not contain corrections for nuclear quantization.

1. $C_2H_5^+$. A complete set of $\alpha_{\mu}^{QC}(\omega)$-spectra are presented in the ESI.† The spectra are computed for a range of total energies, and, as stated earlier, the total energy in these classical AIMD simulations is simply a mechanism to tune-in the requisite degree of anharmonicity. The computed spectra are valid approximations when the energy is within the range of the (unknown) quantized states of the system. Clearly, the harmonic approximation provides an (often very weak) upper bound to the zero-point eigen-energy in such highly anharmonic, fluxional, multi-potential-well systems. In fact, such multi-potential-well systems may also present a critical challenge to many semi-classical methods.[76] Here we study the spectral evolution for a range of total energies, some clearly too low (see ESI,† Fig. SI-1) and some in the range of the harmonic ZPE. As noted in the ESI,† spectra in the range 14.31 kcal mol^{-1} to 21.50 kcal mol^{-1} are relatively consistent and hence in Fig. 11, we present a selected spectrum for $C_2H_5^+$ from this range. For the spectrum presented in Fig. 11 and for the higher-energy spectra in the ESI† (blue spectra in Fig. SI-1), the lower-energy "bridged" structure dominates spectral features, and these

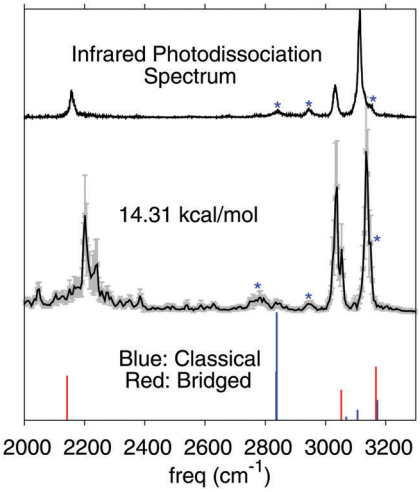

Fig. 11 The central panel contains the computed IR spectrum for $C_2H_5^+$ (frequencies scaled by 0.972) computed using $\alpha_{\mu}^{QC}(\omega)$ (eqn (B2) in Appendix B). The average simulation energy is also noted. The bottom panel displays harmonic spectra for the "bridged" and "classical" structures. The top panels display the results from an argon-tagged action spectroscopy experiment[16] for comparison.

simulations show spectral features that are consistent with the harmonic spectrum of the "classical" (transition state) structure. This is also consistent with the non-negligible "classical" population noted from the quantum reduced dimensional distribution in Fig. 6(a).

While the "classical" spectral features denoted by asterisks in Fig. 11 can be observed through close inspection, the two-dimensional, $\alpha_{\mu}^{QC}(T,\omega;\Delta T)$-spectra shown in Fig. 12 offer a much more compelling picture with regard to population transfer. In the plotted region from 2000 to 2900 cm^{-1}, the center-"bridge" proton stretch of the "bridged" structure is at 2142.20 cm^{-1}, and the symmetric and asymmetric stretches of the CH_3 group of the "classical" structure occur at 2836.02 cm^{-1} and 2838.36 cm^{-1}. (See discussion in ESI† for a detailed discussion on the correspondence between the "classical" and "bridged" harmonic modes.) Thus, by studying the $\alpha_{\mu}^{QC}(T,\omega;\Delta T)$-spectral intensity through the course of dynamics, one can track interconversions between the two geometries by following the aforementioned modes as marked in Fig. 12. (The quantity is defined in Appendix B, see eqn (B3).) Indeed, as the energy of the system is increased, the "classical" structure is populated to a greater extent as indicated by the increasing spectral intensity at approximately 2800 cm^{-1}. For energies too far below the harmonic ZPE, the cyclic structure remains the only contributing structure, as one might expect, but for higher energies, the classical contributions are apparent. In simulations at energies greater than 40 kcal mol^{-1} (which interestingly is close to the harmonic ZPE), broad spectral intensities are seen as is clear from Fig. 12(e). These higher energy spectra are likely to materialize when the system is interrogated using IRMPD.[53–55,72,73]

As discussed earlier, the authors in ref. 17 assign the peaks marked with asterisks in Fig. 9(a) to the impurity $H^+N_2Ar_2$. However, based on our computed spectra from AIMD simulations,

 This journal is © the Owner Societies 2017

Published on 06 September 2017. Downloaded by Indiana University Libraries on 7/27/2018 11:48:17 AM.

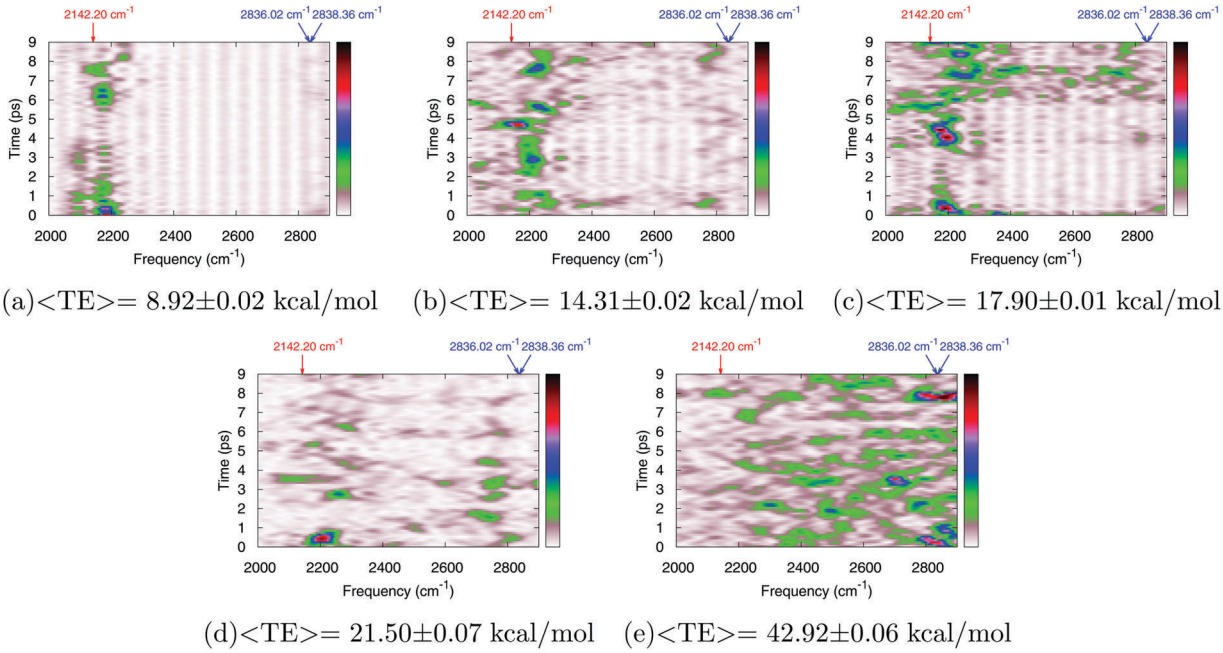

Fig. 12 Two-dimensional time–frequency analysis for $C_2H_5^+$ using $\alpha_\mu^{QC}(T,\omega;\Delta T)$ (eqn (B3)) conducted at average simulation energies noted in the subfigure caption. Frequencies scaled by 0.972. Critical "bridged" and "classical" frequencies are marked to explicate the increasing propensity of appearance of the classical conformer.

where no impurity was added, we note that contributions of the "classical" structure may be an alternative explanation for these minor spectral features. For completeness, we also present harmonic fundamentals and computed spectra for AIMD simulations for $H^+N_2Ar_2$ in the ESI.†

2. **$C_3H_3^+$.** As is the case for $C_2H_5^+$, a full range of spectral properties for $C_3H_3^+$ as a function of simulation total energy is provided in the ESI.† Again, it is clear that the lower energy spectra in red in Fig. SI-4 and SI-5 (ESI†) are relatively consistent and we present a typical spectrum in this range in Fig. 13. The higher energy spectra in Fig. SI-4 and SI-5 (ESI†) demonstrate substantial mode-mixing between the "cyclic" and "straight" conformers and are not relevant for low-energy argon-tagged action spectra experiments, but may be more relevant for IRMPD.

As previously discussed, the spectra for $C_3H_3^+$ are from simulations in which the "straight" structure was used as the initial geometry to best match experimental conditions which

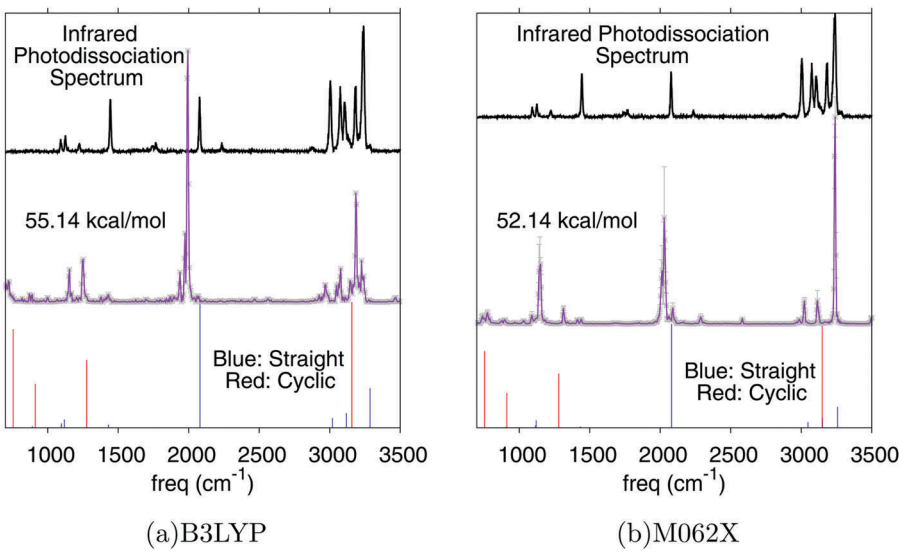

Fig. 13 IR spectra for $C_3H_3^+$ (scaled by 0.972 for M062X and by 0.975 for B3LYP) computed using $\alpha_\mu^{QC}(\omega)$ (eqn (B2) in Appendix B). For the two different basis sets, the simulation was performed with total energy closest to the eigenvalue of the lowest-energy wavefunction with density localized on the "straight" potential well. Contributions from the "cyclic" structure are apparent.

Published on 06 September 2017. Downloaded by Indiana University Libraries on 7/27/2018 11:48:17 AM.

use propargyl bromide as the precursor. Recall that the lowest-energy "straight" eigenstate (Fig. 10) demonstrates non-negligible density in the "cyclic" wells, and, hence, one would expect to see population of this "cyclic" structure under ambient conditions. Unsurprisingly, then, all spectra computed for simulations with a "straight" initial geometry demonstrate some spectroscopic contributions from the lower-energy "cyclic" structure. This explanation is an alternative to the proposition in ref. 16 that the "cyclic" structure is formed through plasma chemistry.

V. Conclusion

A detailed investigation on the fundamental carbocations $C_2H_5^+$ and $C_3H_3^+$ has been conducted. Both species appear to be stabilized by non-classical chemical bonding characterized by delocalization and permutation of hydrogen nuclei over multiple carbon centers through use of a "bridging proton" for $C_2H_5^+$ and a "bridging CH group" for $C_3H_3^+$. This result has been recognized in previous theoretical publications, and, in ref. 32, the similarities between such processes and the well-known "Grotthuss proton shuttle" in water have been deeply analyzed. In this work, we studied the two anomalous carbocation systems by probing (a) their electronic structure-based stability, (b) the effect of the nuclear quantization as manifested through the potential energy surface experienced by the nuclei where all levels of anharmonic behavior are included through use of *ab initio* molecular dynamics, (c) structural stability as dictated by the aforementioned potential surfaces, and (d) analysis of one-dimensional and two-dimensional time–frequency vibrational spectroscopic properties.

In the case of $C_2H_5^+$, we find that the hydrogen nucleus at the bridge position circumscribes the carbon–carbon bond, in the process, permuting positions with the terminal protons. The propensity of this process increases with increasing energy and is very much reminiscent of the delocalization mechanism described in ref. 32 for $C_2H_3^+$ as well as the Grotthuss mechanism[34] for aqueous proton transport. Importantly, at all energies in the vicinity of the quantum nuclear zero-point energy, the axial CH group (represented as "A") migrates and cleaves to allow the appearance of the "propargyl" and then the "straight" configurations for $C_3H_3^+$ during AIMD simulations. The experimental vibrational action spectrum is modeled here through simulations that begin with the "straight" configuration. This is to remain consistent with the experimental conditions that utilize propargyl bromide as the precursor for the creation of $C_3H_3^+$. Classical and quantum nuclear studies both indicate the presence of the "cyclic" structure during our simulations, and hence, the computed vibrational spectra contain signatures from these species as well as additional configurational forms that intervene between the "straight" and "cyclic" forms of $C_3H_3^+$.

Conflicts of interest

There are no conflicts to declare.

Appendix A: a brief discussion of the approximations in eqn (1)

Consider the full nuclear Schrödinger equation across two multi-dimensional variables: $\{\theta;\theta^\perp\}$. (See discussion near eqn (1) for a description of variables.)

$$[T_\theta + T_{\theta^\perp} + V(\theta;\theta^\perp)]\Psi(\theta;\theta^\perp) = E\Psi(\theta;\theta^\perp) \quad \text{(A1)}$$

where T_θ and $T_{\theta^\perp}$ are the respective kinetic energy operators with potential $V(\theta;\theta^\perp)$. If we invoke a mean field approximation across variables $\{\theta;\theta^\perp\}$, we obtain

$$[T_\theta + \tilde{T}_{\theta^\perp} + \tilde{V}(\theta)]\phi(\theta) = E\phi(\theta) \quad \text{(A2)}$$

where $\tilde{T}_{\theta^\perp} \equiv \langle\chi(\theta^\perp)|T_{\theta^\perp}|\chi(\theta^\perp)\rangle$, that is the average kinetic energy from $\theta^\perp$ and

$$\tilde{V}(\theta) \equiv \langle\chi(\theta^\perp)|V(\theta;\theta^\perp)|\chi(\theta^\perp)\rangle \quad \text{(A3)}$$

It is our goal in eqn (1) to approximate the potential in eqn (A3) for use in the reduced dimensional Schrödinger equation, eqn (A2). Details regarding T_θ are discussed in the ESI.† In this publication, we have ignored contributions from $\tilde{T}_{\theta^\perp}$. However, we also note that $\tilde{V}(\theta)$ is an averaged potential and while $V(\theta;\theta^\perp)$ is also known from AIMD data, $\chi(\theta^\perp)$ is not known. We approximate the probability associated with $\chi(\theta^\perp)$ as a Boltzmann distribution and this aspect is clear from eqn (1). Furthermore, the "average" nature of the interaction between θ and $\theta^\perp$ may be further modulated by considering multiple potentials at different values of β in eqn (1). While we have not done this here to gauge the effect on quantum nuclear distributions, we have considered multiple temperatures in our analysis in ESI,† the main features from which are presented in the paper.

Appendix B: velocity and dipole auto-correlation functions to compute spectral intensities and spectral diffusion

The Fourier Transform of Dipole–Dipole Auto-correlation was computed in this study through use of quantum-nuclear corrections[77–79] obtained within the harmonic approximation:

$$\alpha_\mu^{\mathrm{QC}}(\omega) \propto \frac{\omega}{1-\exp(-\beta\hbar\omega)} \times \left\{\omega[1-\exp(-\beta\hbar\omega)]\lim_{T\to\infty}\int_{t=0}^{t=T} \mathrm{d}t \exp(-i\omega t)\langle\mu(0)\cdot\mu(t)\rangle\right\}. \quad \text{(B1)}$$

The terms inside the curly brackets ($\{\cdots\}$) represent the power normalized absorption cross-section.[80,81] The pre-factor, $\frac{\omega}{1-\exp(-\beta\hbar\omega)}$, is a quantum-nuclear correction.[77–79] Over a series of publications[44–48,56,59,82] it has been shown that these correlation functions provide a good estimate of the vibrational spectrum obtained from experimental action spectroscopy.

 This journal is © the Owner Societies 2017

Published on 06 September 2017. Downloaded by Indiana University Libraries on 7/27/2018 11:48:17 AM.

Utilizing the convolution theorem,[83] eqn (B1) may be rewritten as

$$\alpha_{\mu}^{\mathrm{QC}}(\omega) \propto \omega^2 \lim_{T\to\infty} \sum_{i=1}^{3} \left| \int_{t=0}^{t=T} \mathrm{d}t \exp(-i\omega t)\mu_i(t) \right|^2. \quad \text{(B2)}$$

This process of reduction of the dipole auto-correlation function to a power spectrum of dipoles is also known as the Wiener–Khinchin theorem.[83] Furthermore, when a finite sample of data is constructed, as in eqn (B2), there is always a leakage (or smudging phenomenon) where information from one frequency leaks to the neighboring frequency regions of the spectrum. The extent of leakage falls as $1/\omega^2$. To overcome this problem, we follow ref. 83, and use the method of overlapping segments to construct the Fourier transform in eqn (B2). Thus, for all simulations, we compute $\alpha_{\mu}^{\mathrm{QC}}(\omega)$ using dynamics data from 0–3 ps, 0.2–3.2 ps, *etc.*, for all trajectories. The results are averaged with standard deviations provided as error-bars in Fig. 11 and 13.

For the study of two-dimensional time–frequency analysis, eqn (B2) can be modified to calculate the time–frequency function:

$$\alpha_{\mu}^{\mathrm{QC}}(T,\omega;\Delta T) \propto \omega^2 \sum_{i=1}^{3} \left| \int_{t=0}^{t=T} \mathrm{d}t\omega(t;T,\Delta T) \exp(-i\omega t)\mu_i(t) \right|^2. \quad \text{(B3)}$$

where $\omega(t;T,\Delta T)$ is a window function centered at T with width ΔT. But if the amount of energy in a certain spectral range is to be computed as a function of time, we may utilize a similar expression as that above,[84] by replacing the instantaneous dipoles with instantaneous nuclear velocities, $\boldsymbol{\mathcal{V}}_{i,j}(t)$, to obtain

$$\alpha_{\mathrm{V}}(T,\omega;\Delta T) \propto \sum_{i=1}^{N_{\mathrm{Atoms}}} \sum_{j=1}^{3} \left| \int_{t=0}^{t=T} \mathrm{d}t\omega(t;T,\Delta T) \exp(-i\omega t)\boldsymbol{\mathcal{V}}_{i,j}(t) \right|^2. \quad \text{(B4)}$$

In the current study, ΔT is set to 500 fs; the window function is chosen as a step function; and smoothing techniques such as those discussed in ref. 84 have not been employed.

Acknowledgements

This research is supported by the National Science Foundation grant NSF CHE-1665336 to SSI. LMS is a Goldwater fellow and an ACS undergraduate physical chemistry fellow, and she is supported by the Cox Research Scholarship Foundation at Indiana University. We thank Professor Michael Duncan for sharing with us data from ref. 16 and 17.

References

1 G. K. S. Prakash and P. v. R. Schleyer, *Stable Carbocation Chemistry*, John Wiley and Sons, New York, 1997.
2 G. A. Olah and G. K. S. Prakash, *Carbocation Chemistry*, John Wiley and Sons, Hoboken, NJ, 2004.
3 J. L. Holmes, C. Aubry and P. M. Mayer, *Assigning structures to ions in mass spectrometry*, CRC Press, Taylor Francis Group, New York, 2006.
4 G. A. Olah, T. Mathew and G. K. S. Prakash, Relevance and Significance of Extraterrestrial Abiological Hydrocarbon Chemistry, *J. Am. Chem. Soc.*, 2016, **138**, 6905.
5 J. M. Greenberg and V. Pirronello, *Chemistry in Space*, Kluwer Academic Publishers, Dordrecht, 1991.
6 A. E. Glassgold, A. Omont and M. Guélin, Protonated Acetylene – An Important Circumstellar And Interstellar Ion, *Astrophys. J.*, 1992, **396**, 115.
7 P. Gutta and D. J. Tantillo, Proton Sandwiches: Nonclassical Carbocations with 4-Coordinate Protons, *Angew. Chem., Int. Ed.*, 2005, **44**, 2719–2723.
8 P. Gutta and D. J. Tantillo, A Promiscuous Proton in Taxadiene Biosynthesis?, *Org. Lett.*, 2007, **9**, 1069–1071.
9 D. H. Aue, Carbocations, *Wiley Interdiscip. Rev.: Comput. Mol. Sci.*, 2011, **1**, 487.
10 Y. J. Hong and D. J. Tantillo, Feasibility of Intramolecular Proton Transfers in Terpene Biosynthesis – Guiding Principles, *J. Am. Chem. Soc.*, 2015, **137**, 4134–4140.
11 C. M. Gabrys, D. Uy, M.-F. Jagod, T. Oka and T. Amano, Infrared Spectroscopy of Carboions. 8. Hollow Cathode Spectroscopy of Protonated Acetylene, $C_2H_3^+$, *J. Phys. Chem.*, 1995, **99**, 15611.
12 J. T. Hougen and L. H. Coudert, Reexamination of the $C_2H_3^+$ microwave and infrared spectra, *J. Mol. Spectrosc.*, 2011, **270**, 123.
13 M. Bogey, H. Bolvin, M. Cordonnier, C. Demuynck, J. L. Destombes, R. Escribano and P. C. Gomez, Tunneling splittings in the rotational spectrum of $C_2H_3^+$, *Can. J. Phys.*, 1994, **72**, 967.
14 G. E. Douberly, A. M. Ricks, B. W. Ticknor, W. C. McKee, P. v. R. Schleyer and M. A. Duncan, Infrared Photodissociation Spectroscopy of Protonated Acetylene and Its Clusters, *J. Phys. Chem. A*, 2008, **112**, 1897.
15 M. A. Duncan, Infrared Laser Spectroscopy of Mass-Selected Carbocations, *J. Phys. Chem. A*, 2012, **116**, 11477.
16 A. M. Ricks, G. E. Douberly, P. v. R. Schleyer and M. A. Duncan, Communications: infrared spectroscopy of gase phase $C_3H_3^+$ ions: the cyclopropenyl and propargyl cations, *J. Chem. Phys.*, 2010, **132**, 0501101.
17 A. M. Ricks, G. E. Douberly, P. v. R. Schleyer and M. A. Duncan, Infrared spectroscopy of protonated ethylene: the nature of proton binding in the non-classical structure, *Chem. Phys. Lett.*, 2009, **480**, 17–20.
18 H. S. Andrei, N. Solca and O. Dopfer, IR Spectrum of the Ethyl Cation: Evidence for the Nonclassical Structure, *Angew. Chem., Int. Ed.*, 2008, **47**, 395.
19 E. P. Kanter, Z. Vager, G. Both and D. Zajfman, A measurement of the low energy stereostructure of protonated acetylene, $C_2H_3^+$, *J. Chem. Phys.*, 1986, **85**, 7487.
20 Z. Vager, D. Zajfman, T. Graber and E. P. Kanter, Experimental evidence for anomalous nuclear delocalization in $C_2H_3^+$, *Phys. Rev. Lett.*, 1993, **71**, 4319.
21 W. Klopper and W. Kutzelnigg, MP2-R12 Calculations on the Relative Stability of Carbocations, *J. Phys. Chem.*, 1990, **94**, 5625.

Published on 06 September 2017. Downloaded by Indiana University Libraries on 7/27/2018 11:48:17 AM.

22 K. Raghavachari, R. A. Whiteside, J. A. Pople and P. v. R. Schleyer, Molecular orbital theory of the electronic structure of organic molecules. 40. Structures and energies of C1–C3 carbocations including effects of electron correlation, *J. Am. Chem. Soc.*, 1981, **103**, 5649.

23 P. C. Hariharan, W. A. Lathan and J. A. Pople, Molecular orbital theory of simple carbonium ions, *Chem. Phys. Lett.*, 1972, **14**, 385.

24 B. Zurawski, R. Ahlrichs and W. Kutzelnigg, Have the ions $C_2H_3^+$ and $C_2H_5^+$ classical or non-classical structure?, *Chem. Phys. Lett.*, 1973, **21**, 309.

25 J. Weber, M. Yoshimine and A. D. McLean, A CI study of the classical and nonclassical structures of the vinyl cation and their optimum path for rearrangement, *J. Chem. Phys.*, 1976, **64**, 4159.

26 H. Lischka and H. J. Koehler, Structure and stability of the carbocations $C_2H_3^+$ and $C_2H_4X^+$, X = hydrogen, fluorine, chlorine, and methyl. Ab initio investigation including electron correlation and a comparison with MINDO/3 results, *J. Am. Chem. Soc.*, 1978, **100**, 5297.

27 D. Marx and M. Parrinello, The Effect Of Quantum And Thermal Fluctuations On The Structure Of The Floppy Molecule $C_2H_3^+$, *Science*, 1996, **271**, 179.

28 L. Knoll, Z. Vager and D. Marx, Experimental Versus Simulated Coulomb-Explosion Images Of Flexible Molecules: Structure Of Protonated Acetylene $C_2H_3^+$, *Phys. Rev. A: At., Mol., Opt. Phys.*, 2003, **67**, 022506.

29 A. R. Sharma, J. Wu, B. J. Braams, S. Carter, R. Schneider, B. Shepler and J. M. Bowman, Potential Energy Surface and MULTIMODE Vibrational Analysis of $C_2H_3^+$, *J. Chem. Phys.*, 2006, **125**, 224306.

30 B. T. Psciuk, V. A. Benderskii and H. B. Schlegel, Protonated Acetylene Revisited, *Theor. Chem. Acc.*, 2007, **118**, 75.

31 R. C. Fortenberry, X. Huang, T. D. Crawford and T. J. Lee, Quartic Force Field Rovibrational Analysis Of Protonated Acetylene, $C_2h_3^+$, and its Isotopologues, *J. Phys. Chem. A*, 2014, **118**, 7034.

32 J. Li, A. B. Pacheco, K. Raghavachari and S. S. Iyengar, A Grotthuss-like proton shuttle in the anomalous $C_2H_3^+$ carbocation: energetic and vibrational properties for isotopologues, *Phys. Chem. Chem. Phys.*, 2016, **18**, 29395.

33 A. R. Sharma, B. J. Braams, S. Carter, B. C. Shepler and J. M. Bowman, Full-Dimensional *ab initio* Potential Energy Surface and Vibrational Configuration Interaction Calculations for Vinyl, *J. Chem. Phys.*, 2009, **130**, 174301.

34 N. Agmon, The Grotthuss Mechanism, *Chem. Phys. Lett.*, 1995, **244**, 456.

35 S. A. Perera and R. J. Bartlett, Predicted NMR Coupling Constants and Spectra for Ethyl Carbocation: A Fingerprint for Nonclassical Hydrogen-Bridged Structures, *J. Am. Chem. Soc.*, 1995, **117**, 8476.

36 M. W. Wong and L. Radom, Multiply Charged Isoelectronic Analogues of $C_3H_3^+$: Cyclic or Open Chain?, *J. Am. Chem. Soc.*, 1989, **111**, 6976.

37 X. Huang, P. R. Taylor and T. J. Lee, Highly Accurate Quartic Force Fields, Vibrational Frequencies, and Spectroscopic Constants for Cyclic and Linear $C_3H_3^+$, *J. Phys. Chem. A*, 2011, **115**, 5005.

38 F. P. Lossing, Free Radicals by Mass Spectrometry. XLV. Ionization Potentials and Heats of Formation of $C_3H_3^+$, $C_3H_5^+$, and $C_4H_7^+$ Radicals and Ions, *Can. J. Chem.*, 1972, **50**, 3973.

39 J. Li and S. S. Iyengar, *Ab initio* Molecular Dynamics using Recursive, Spatially Separated, Overlapping Model Subsystems Mixed Within an ONIOM Based Fragmentation Energy Extrapolation Technique, *J. Chem. Theory Comput.*, 2015, **11**, 3978–3991.

40 J. Li, C. Haycraft and S. S. Iyengar, Hybrid extended Lagrangian, post-Hartree-Fock Born-Oppenheimer *ab initio* molecular dynamics using fragment-based electronic structure, *J. Chem. Theory Comput.*, 2016, **12**, 2493.

41 C. Haycraft, J. Li and S. S. Iyengar, ''On-the-fly'' *Ab initio* molecular dynamics with coupled cluster accuracy, *J. Chem. Theory Comput.*, 2017, **13**, 1887.

42 Y. Zhao and D. Truhlar, The M06 suite of density functionals for main group thermochemistry, thermochemical kinetics, noncovalent interactions, excited states, and transition elements: two new functionals and systematic testing of four M06-class functionals and 12 other functionals, *Theor. Chem. Acc.*, 2006, **120**, 215.

43 A. D. Becke, Density-Functional Thermochemistry. 3. The Role of Exact Exchange, *J. Chem. Phys.*, 1993, **98**, 5648.

44 S. S. Iyengar, Further Analysis of the Dynamically Averaged Vibrational Spectrum for the ''Magic'' Protonated 21-Water Cluster, *J. Chem. Phys.*, 2007, **126**, 216101.

45 S. S. Iyengar, M. K. Petersen, T. J. F. Day, C. J. Burnham, V. E. Teige and G. A. Voth, The Properties of Ion-Water Clusters. I. the Protonated 21-Water Cluster, *J. Chem. Phys.*, 2005, **123**, 084309.

46 X. Li, J. Oomens, J. R. Eyler, D. T. Moore and S. S. Iyengar, Isotope Dependent, Temperature Regulated, Energy Repartitioning in a Low-Barrier, Short-Strong Hydrogen Bonded Cluster, *J. Chem. Phys.*, 2010, **132**, 244301.

47 S. M. Dietrick and S. S. Iyengar, Constructing Periodic Phase Space Orbits from *Ab Initio* Molecular Dynamics Trajectories to Analyze Vibrational Spectra: Case Study of the Zundel ($H_5O_2^+$) Cation, *J. Chem. Theory Comput.*, 2012, **8**, 4876.

48 X. Li, V. E. Teige and S. S. Iyengar, Can the Four-Coordinated, Penta-Valent Oxygen in Hydroxide Water Clusters Be Detected Through Experimental Vibrational Spectroscopy?, *J. Phys. Chem. A*, 2007, **111**, 4815.

49 D. S. Bomse, R. L. Woodin and J. L. Beauchamp, Molecular Activation with Low-Intensity CW Infrared-Laser Radiation - Multi-Photon Dissociation of Ions Derived from Diethyl-Ether, *J. Am. Chem. Soc.*, 1979, **101**, 5503.

50 G. J. Diebold, F. Engelke, D. M. Lubman, J. C. Whitehead and R. N. Zare, Infrared Multiphoton Dissociation of SF_6 in a Molecular-Beam – Observation of F-Atoms by Chemi-Ionization Detection, *J. Chem. Phys.*, 1977, **67**, 5407.

51 E. R. Grant, M. J. Coggiola, Y. T. Lee, P. A. Schulz, A. S. Sudbo and Y. R. Shen, Extent of Energy Randomization in Infrared Multiphoton Dissociation of SF_6, *Chem. Phys. Lett.*, 1977, **52**, 595.

 This journal is © the Owner Societies 2017

Published on 06 September 2017. Downloaded by Indiana University Libraries on 7/27/2018 11:48:17 AM.

52 J. Oomens, B. G. Sartakov, G. Meijer and G. Von Helden, Gas-Phase Infrared Multiple Photon Dissociation Spectroscopy of Mass-Selected Molecular Ions, *Int. J. Mass Spectrom.*, 2006, **254**, 1.

53 J. J. Valle, J. R. Eyler, J. Oomens, D. T. Moore, A. F. G. van der Meer, G. von Helden, G. Meijer, C. L. Hendrickson, A. G. Marshall and G. T. Blakney, Free Electron Laser-Fourier Transform Ion Cyclotron Resonance Mass Spectrometry Facility for Obtaining Infrared Multiphoton Dissociation Spectra of Gaseous Ions, *Rev. Sci. Instrum.*, 2005, **76**, 023103.

54 K. R. Asmis, N. L. Pivonka, G. Santambrogio, M. Brümmer, C. Kaposta, D. M. Neumark and L. Wöste, Gas-Phase Infrared Spectrum of the Protonated Water Dimer, *Science*, 2003, **299**, 1375.

55 M. F. Bush, M. W. Forbes, R. A. Jockusch, J. Oomens, N. C. Polfer, R. Saykally and E. Williams, Infrared Spectroscopy of Cationized Lysine and E-*N*-Methyl Lysine in the Gas Phase: Effects of Alkali Metal Ion Size and Proton Affinity on Zwitterion Stability, *J. Phys. Chem. A*, 2007, **111**, 7753.

56 X. Li, D. T. Moore and S. S. Iyengar, Insights from First Principles Molecular Dynamics Studies Towards Infra-Red Multiple-Photon and Single-Photon Action Spectroscopy: Case Study of the Proton-Bound Di-Methyl Ether Dimer, *J. Chem. Phys.*, 2008, **128**, 184308.

57 X. Shi, W. Li and H. B. Schlegel, Computational simulations of hydrogen circular migration in protonated acetylene induced by circularly polarized light, *J. Chem. Phys.*, 2016, **145**, 084309.

58 I. Sumner and S. S. Iyengar, Quantum Wavepacket *Ab Initio* Molecular Dynamics: An Approach for Computing Dynamically Averaged Vibrational Spectra Including Critical Nuclear Quantum Effects, *J. Phys. Chem. A*, 2007, **111**, 10313.

59 S. S. Iyengar, Dynamical Effects on Vibrational and Electronic Spectra of Hydroperoxyl Radical Water Clusters, *J. Chem. Phys.*, 2005, **123**, 084310.

60 S. S. Iyengar and J. Jakowski, Quantum Wavepacket *Ab Initio* Molecular Dynamics: An Approach to Study Quantum Dynamics in Large Systems, *J. Chem. Phys.*, 2005, **122**, 114105.

61 J. Jakowski, I. Sumner and S. S. Iyengar, Computational Improvements to Quantum Wavepacket *Ab Initio* Molecular Dynamics Using a Potential-Adapted, Time-Dependent Deterministic Sampling Technique, *J. Chem. Theory Comput.*, 2006, **2**, 1203.

62 Y. Huang, D. J. Kouri, M. Arnold, I. T. L. Marchioro and D. K. Hoffman, Distributed Approximating Function Approach to Time-Dependent Wavepacket Propagation in 3-Dimensions: Atom-Surface Scattering, *Comput. Phys. Commun.*, 1994, **80**, 1.

63 D. J. Kouri, Y. Huang and D. K. Hoffman, Iterated Real-Time Path Integral Evaluation Using a Distributed Approximating Functional Propagator and Average-Case Complexity Integration, *Phys. Rev. Lett.*, 1995, **75**, 49.

64 G. Liu, Z. Li, Y. Ding, Q. Fu, X. Huang, C. Sun and A. Tang, Water-Assisted Isomerization from Linear Propargylium (H_2CCCH^+) to Cyclopropenylium (c-$C_3H_3^+$), *J. Phys. Chem. A*, 2002, **106**, 10415–10422.

65 J. M. Bowman, The Self-Consistent-Field Approach to Polyatomic Vibrations, *Acc. Chem. Res.*, 1986, **19**, 202.

66 J. O. Jung and R. B. Gerber, Vibrational Wave Functions and Spectroscopy of $(H_2O)(N)$, N = 2, 3, 4, 5: Vibrational Self-Consistent Field with Correlation Corrections, *J. Chem. Phys.*, 1996, **105**, 10332.

67 R. B. Gerber and M. A. Ratner, Self-Consistent-Field Methods for Vibrational Excitations in Polyatomic Systems, *J. Chem. Phys.*, 1988, **70**, 97.

68 N. Matsunaga, G. M. Chaban and R. B. Gerber, Degenerate Perturbation Theory Corrections for the Vibrational Self-Consistent Field Approximation: Method and Applications, *J. Chem. Phys.*, 2002, **117**, 3541.

69 T. J. Lee, J. E. Rice and H. F. Schaeffer, The infrared spectrum of the acetylene radical cation $C_2H_2^+$. A theoretical study using SCF, MCSCF, and CI methods, *J. Chem. Phys.*, 1987, **85**, 3051–3053.

70 R. C. Fortenberry, X. Huang, T. D. Crawford and T. J. Lee, Quartic Force Field Rovibrational Analysis of Protonated Acetylene, $C_2H_3^+$, and Its Isotopologues, *J. Phys. Chem. A*, 2014, **118**, 7034–7043.

71 C. Swalina and S. Hammes-Schiffer, Impact of Nuclear Quantum Effects on the Molecular Structure of Bihalides and the Hydrogen Fluoride Dimer, *J. Phys. Chem. A*, 2005, **109**, 10410.

72 D. T. Moore, J. Oomens, L. van der Meer, G. von Helden, G. Meijer, J. Valle, A. G. Marshall and J. R. Eyler, Probing the Vibrations of Shared, OH^+O-Bound Protons in the Gas Phase, *ChemPhysChem*, 2004, **5**, 740.

73 N. L. Pivonka, C. Kaposta, M. Brummer, G. von Helden, G. Meijer, L. Woste, D. M. Neumark and K. R. Asmis, Probing a Strong Hydrogen Bond with Infrared Spectroscopy: Vibrational Predissociation of $BrHBr^-$·Ar, *J. Chem. Phys.*, 2003, **118**, 5275.

74 J. R. Roscioli, L. R. McCunn and M. A. Johnson, Quantum Structure of the Intermolecular Proton Bond, *Science*, 2007, **316**, 249.

75 J. M. Headrick, E. G. Diken, R. S. Walters, N. I. Hammer, R. A. Christie, J. Cui, E. M. Myshakin, M. A. Duncan, M. A. Johnson and K. Jordan, Spectral Signatures of Hydrated Proton Vibrations in Water Clusters, *Science*, 2005, **308**, 1765.

76 R. Conte, A. Aspuru-Guzik and M. Ceotto, Reproducing Deep Tunneling Splittings, Resonance, and Quantum Frequencies in Vibrational Spectra From a Handful of Direct *Ab Initio* Semiclassical Trajectories, *J. Phys. Chem. Lett.*, 2013, **4**, 3407–3412.

77 P. H. Berens, S. R. White and K. R. Wilson, Molecular Dynamics and Spectra. II. Diatomic Raman, *J. Chem. Phys.*, 1981, **75**, 515.

78 J. S. Bader and B. J. Berne, Quantum and Classical Relaxation Rates from Classical Simulations, *J. Chem. Phys.*, 1994, **100**, 8359.

79 C. P. Lawrence, A. Nakayama, N. Makri and J. L. Skinner, Quantum Dynamics in Simple Fluids, *J. Chem. Phys.*, 2004, **120**, 6621.

Published on 06 September 2017. Downloaded by Indiana University Libraries on 7/27/2018 11:48:17 AM.

80 R. G. Gordon, Correlation Functions for Molecular Motion, *Adv. Magn. Reson.*, 1968, **3**, 1.
81 D. A. McQuarrie, *Statistical Mechanics*, University Science Books, Sausalito, CA, 2000.
82 D. Vimal, A. B. Pacheco, S. S. Iyengar and P. S. Stevens, Experimental and Ab Initio Dynamical Investigations of the Kinetics and Intramolecular Energy Transfer Mechanisms for the OH + 1,3-Butadiene Reaction Between 263 and 423 K at Low Pressure, *J. Phys. Chem. A*, 2008, **112**, 7227.
83 W. H. Press, S. A. Teukolsky, W. T. Vetterling and B. P. Flannery, *Numerical Recipes in C*, Cambridge University Press, New York, 1992.
84 S. M. Dietrick, A. B. Pacheco, P. Phatak, P. S. Stevens and S. S. Iyengar, The Influence of Water on Anharmonicity, Stability and Vibrational Energy Distribution of Hydrogen-Bonded Adducts in Atmospheric Reactions: Case Study of the OH + Isoprene Reaction Intermediate Using *Ab-Initio* Molecular Dynamics, *J. Phys. Chem. A*, 2012, **116**, 399.

 This journal is © the Owner Societies 2017